Unsteady Aerodynamic Simulation of Multiple Bodies in Relative Motion: A Prototype Method

Robert L. Meakin

NASA

National Aeronautics and
Space Administration

Unsteady Aerodynamic Simulation of Multiple Bodies in Relative Motion: A Prototype Method

Robert L. Meakin, Sterling Federal Systems, Inc.,
Ames Research Center, Moffett Field, California

July 1989

UNSTEADY AERODYNAMIC SIMULATION OF MULTIPLE BODIES IN RELATIVE MOTION: A PROTOTYPE METHOD

Robert L. Meakin

Sterling Federal Systems, Inc.

NASA Ames Research Center, Moffett Field, California

Abstract

A prototype method for time-accurate simulation of multiple aerodynamic bodies in relative motion is presented. The method is general and features unsteady chimera domain decomposition techniques and an implicit approximately factored finite-difference procedure to solve the time-dependent thin-layer Navier-Stokes equations. The method is applied to a set of two- and three-dimensional test problems to establish spatial and temporal accuracy, quantify computational efficiency, and begin to test overall code robustness.

I. INTRODUCTION

Advances in computer hardware design and numerical algorithm improvements continue to broaden the horizon of solvable fluid dynamic problems via computational means. There has long been interest in unsteady multiple body aerodynamics: separation of payloads and spent external fuel tanks from high performance aircraft, separation of the space shuttle orbiter from its giant external fuel tank and solid rocket boosters, and ground/aircraft interaction during take-off and landing of STOVL aircraft are among numerous applications from the past and present. The value of computational analysis for such flow regimes is evident when considering the limitations of conventional wind tunnel testing, and the high cost and hazards associated with flight testing. It has been only recently, however, that this class of flows has become a tractable candidate for CFD, though it is still computationally expensive.

The present paper describes a prototype method intended for time accurate simulation of three-dimensional multiple body viscous flows (subsonic, transonic, and supersonic) given arbitrary grid combinations, body shapes, and relative motion between grid systems. The method is intended primarily for the duration of time wherein there exists aerodynamic influence between primary and subordinate moving bodies. It is expected that once moving bodies are beyond the immediate aerodynamic influence of the primary bodies, conventional engineering methods would be employed. The method is composed of three major Functions, which are, topically speaking, AeroDynamics (ADF), Body Dynamics (BDF), and Domain Connectivity (DCF). At maturity, the method will execute optimized code for each of these functions, and provide overall logic control for the simulations, including an allowance for functional interaction. Presently, the major functions and overall logic control are in varying stages of development and sophistication. Accordingly, delineation of future areas for algorithm development is a secondary objective of this paper. Results are presented which demonstrate the time accuracy of the ADF (i.e., the flow solver), and the ability of the overall prototype method to reproduce wind-tunnel experiments of a generic, but physically realistic, three-dimensional multiple body configuration. Finally, results from two different hypothetical unsteady multiple moving body computations for geometrically complex configurations are presented.

The development of techniques to generate grids and solve the equations of motion for geometrically complex domains has been a pacing item in CFD for several years. As it turns out, a very old idea has been exploited in a variety of ingenious ways to treat flows in complicated three-dimensional domains. The principle is domain decomposition, solving partial differential equations on overlapping subdomains, and was first introduced by Schwarz in about 1860 as an analytic method[1]. Fundamentally, the principle is to split global domains into several overlapping subdomains, and, according to some prescribed sequence, solve the governing system of differential equations on each of the subdomains. Physical boundary conditions are enforced as usual (e.g., no-slip conditions at solid surfaces), while inter-subdomain boundary conditions are obtained from solutions in neighboring subdomains that are overlapped by the boundary in question. The solution sequence is repeated iteratively to facilitate free transfer of information between all subdomains, and to drive the overall solution to convergence.

The particular domain decomposition method adopted in this work, and another similar research effort (see refs. [2,3]), is the "chimera" approach[4]. The basic difference between chimera and other Schwarz descendants [see, for example, 5,6,7,8], is best seen when subdomains are constructed about multiple bodies in close formation. Consider, for example, the flapped airfoil configuration shown in Figures 1 and 2. The problem domain is decomposed into a primary and subordinate pair of subdomains, cor-

responding to the airfoil and flap, respectively. The airfoil subdomain completely overlaps the subordinate flap subdomain. Clearly, conditions for the flap subdomain outer boundaries can be interpolated from the airfoil subdomain, thereby providing the needed airfoil-to-flap subdomain link for information transfer. It is also clear that a similar transfer of information from the flap subdomain back to the airfoil subdomain is required. However, the airfoil subdomain has no "natural" boundaries (physical or conventional inter-subdomain) that overlap the flap subdomain. Chimera makes it possible to create an artificial boundary (hole boundary) within the airfoil subdomain, and thereby establish the required flap-to-airfoil link for information transfer. A hole boundary for this case is created by excluding the region of the airfoil subdomain that is overlapped by a portion of the flap subdomain (including the flap itself). The resulting hole region is excluded from the flow solution of the remaining airfoil subdomain. Conditions for the hole boundary in the airfoil subdomain are interpolated from the flap subdomain. In general, one-way communication links can be established between any pair of subdomains through hole and conventional inter-subdomain boundaries. It is the logic inherent in chimera that allows bodies to create holes in neighboring subdomains that sets it apart from other domain decomposition methods, and makes multiple moving body computations possible.

II. COMPUTATIONAL METHOD

Aerodynamic Function (ADF)

An implicit approximately factored algorithm for the thin-layer Navier Stokes equations has been adopted as the ADF (e.g., the flow solver) for this work. The algorithm uses central differencing in the η and ζ directions and upwinding in ξ. The algorithm is formally presented in references [9,10, and 11], however, for completeness, a brief description is presented here. Employing the thin-layer approximation, the conservation equations for mass, momentum, and energy can be written in nondimensional form for a general curvilinear coordinate system, as

$$\partial_\tau \widehat{Q} + \partial_\xi \widehat{F} + \partial_\eta \widehat{G} + \partial_\zeta \widehat{H} = Re^{-1}\partial_\zeta \widehat{S} \qquad (1)$$

where the viscous terms in ζ have been collected into the vector $\widehat{S}$, and

$$\widehat{Q} = \begin{bmatrix} \rho \\ \rho u \\ \rho v \\ \rho w \\ e \end{bmatrix},$$

$$\widehat{F} = J^{-1} \begin{bmatrix} \rho U \\ \rho u U + \xi_x p \\ \rho v U + \xi_y p \\ \rho w U + \xi_z p \\ (\epsilon + p)U - \xi_t p \end{bmatrix},$$

$$\widehat{G} = J^{-1} \begin{bmatrix} \rho V \\ \rho u V + \eta_x p \\ \rho v V + \eta_y p \\ \rho w V + \eta_z p \\ (\epsilon + p)V - \eta_t p \end{bmatrix},$$

$$\widehat{H} = J^{-1} \begin{bmatrix} \rho W \\ \rho u W + \zeta_x p \\ \rho v W + \zeta_y p \\ \rho w W + \zeta_z p \\ (\epsilon + p)W - \zeta_t p \end{bmatrix}$$

where $U, V,$ and W are unscaled contravariant velocities, for example,

$$U = \xi_t + \xi_x u + \xi_y v + \xi_z w,$$

and the metric Jacobian, J^{-1}, is defined in the usual way.

The numerical analog of equation (1) adopted in this work can be written as

$$\left[I + i_b h \delta_\xi^b (\widehat{A}^+)^n + i_b h \delta_\zeta \widehat{C}^n - i_b h Re^{-1} \bar{\delta}_\zeta J^{-1} \widehat{M}^n J - i_b D_i|_\zeta \right]$$
$$\times \left[I + i_b h \delta_\xi^f (\widehat{A}^-)^n + i_b h \delta_\eta \widehat{B}^n - i_b D_i|_\eta \right] \Delta \widehat{Q}^n =$$
$$-i_b \Delta t \{ \delta_\xi^b (\widehat{F}^+)^n + \delta_\xi^f (\widehat{F}^-)^n + \delta_\eta \widehat{G}^n + \delta_\zeta \widehat{H}^n - Re^{-1}\bar{\delta}_\zeta \widehat{S}^n \}$$
$$-i_b (D_e|_\eta + D_e|_\zeta)\widehat{Q}^n \qquad (2)$$

where $h = \Delta t$ or $(\Delta t)/2$ for first or second order time accuracy. Here, δ is a three-point second order accurate central difference operator, and $\bar{\delta}$ is a midpoint operator used with the viscous terms. The flux F is eigensplit to facilitate use of the forward spacial difference operators δ_ξ^b and δ_ξ^f. The flux differences themselves are midpoint differenced, and backward or forward weights of the split fluxes are used in the manner of Thomas, et al.[12]. The matrices $\widehat{A}, \widehat{B}, \widehat{C},$ and $\widehat{M}$ result from local linearization of the fluxes about the previous time level. D_e and D_i are dissipation operators, and are used in the central space differencing directions.

The only evidence in algorithm (2) of dependence of the ADF on the BDF and DCF is the i_b array. In conventional chimera (static grid) applications, the i_b array

2

facilitates hole boundary logic. That is, grid points which lie within a body (or a specified boundary zone) of another grid, are not allowed to influence the solution of algorithm (2). To negate the effect of such points, the i_b array takes on values of either 1 (for conventional field points) or 0 (for hole points). Hence, the dissipation terms and h in algorithm (2) are multiplied by i_b. Thus, when $i_b = 0$, the algorithm reduces to $\Delta \hat{Q}^n = 0$, or $\hat{Q}^{n+1} = \hat{Q}^n$, leaving $\hat{Q}$ unchanged at hole points. The set of grid points which define the border between conventional field points and chimera "hole points" are called "interpolated boundary points." These points are treated as inter-subdomain boundaries, and likewise depend on solutions in an overlapping grid system(s) for their value of $\hat{Q}$. Values for the i_b array and the interpolation coefficients needed to update the interpolated boundary points are provided by a separate algorithm [13].

In the present study, problems involving multiple bodies in relative motion are being considered. This means that the location of hole and inter-subdomain boundaries are time dependent. Accordingly, the i_b array and required interpolation coefficients are also a function of time. Herein lies the close interdependence of the prototype method's three functional parts for moving body problems. The ADF depends on the DCF to supply hole and interpolation information. The DCF in turn, depends on the BDF to supply the location and orientation of all moving bodies relative to the primary body, or set of bodies. Completing the cycle, the BDF depends on the ADF to provide aerodynamic loads and moments on the moving bodies, in order to perform its function.

Body Dynamics Function (BDF)

The BDF in the prototype method is presently the least developed of the three main functions. Trajectories have been prescribed in the multiple moving body cases simulated thus far. The assumption has been that the ADF would provide the unsteady multiple body flow fields, from which conventional routines could be employed to compute dynamic loadings and moments. These would then be used to predict trajectories, resulting body locations, and attitudes.

In principle, it will not be difficult to add this function to the prototype method as it matures. However, there are some practical issues that must be resolved in order to insure accurate trajectory predictions. The ADF can be depended on to provide accurate predictions of lift and moments on aerodynamic bodies. However, because of memory and cpu time constraints, it will be a long time before CFD (the ADF) can be expected to efficiently provide accurate drag predictions for 3D separated flows. Accordingly, given the quantities that CFD can provide, a suitable model must be developed to accurately predict body trajectories and attitudes.

Domain Connectivity Function (DCF)

The DCF of the prototype method is a modified version of the PEGASUS code developed at AEDC[13]. PEGASUS establishes all of the linkages between grids that will be needed by the ADF. These include determination of interpolation coefficients, and the setting up of chimera logic for bodies making holes in overlapping grids. The code is general and can perform this function on arbitrary configurations of three-dimensional grid systems.

The original PEGASUS was not designed for moving grid configurations. Though nothing prohibits its use for such cases, it is simply not practical. Relative to the cost of a converged steady-state solution, PEGASUS is economical. This is especially true if the grid system can be used for a variety of cases (e.g., Mach numbers, angles of attack, etc.). However, for unsteady moving grid cases, the DCF must be executed each time-step. Depending on the grid configuration, PEGASUS can be many times more expensive than a corresponding ADF iteration. Consider, for example, the results depicted in Table 1 for 2 three-dimensional test problems. The first application corresponds to a minor body of revolution falling away from a generic wing. The second application is for the integrated Space Shuttle vehicle during solid rocket booster (SRB) separation. PEGASUS cost nearly twice the cpu time per iteration as the ADF for the wing body separation case, and more than 5 times the cpu time per iteration as the ADF in the space shuttle SRB separation case.

In the present work PEGASUS has been modified to facilitate a more efficient application of the algorithm for unsteady problems. The new unsteady PEGASUS will be henceforth referred to as the DCF. The main improvement of the DCF over PEGASUS is that it uses a knowledge of hole and inter-subdomain boundary condition locations at time level n to limit its search regions for finding their corresponding locations at time level $n + 1$. In the case of the flapped airfoil considered earlier, if the flap grid is moving, the hole in the airfoil grid needs to be updated for each movement of the flap. In conventional static grid applications of PEGASUS, the hole definition process is typically the most time consuming task performed. In the present DCF, cpu time is grately reduced for moving body cases by limiting the search for time level $n+1$ hole points to the points on either side of the time level n hole boundaries. Technically speaking, this search restriction limits movement of the holes (or moving bodies) during a time-step, because it is necessary to keep hole points from being in-

troduced into the flow field without first being updated as interpolated hole boundary points. In practice, the time-step sizes required to accurately resolve the physical processes

Table 1
Ratios of Domain Connectivity Function versus Aerodynamic Function (cpu time per iter.)

Application	PEG[†]/ADF	DCF/ADF
Wing body separation	1.96	0.64
domains: 2		
points: 243,906		
interpolated boundary		
points: 2,090		
Space Shuttle SRB Separation	5.27	2.02
domains: 3		
points: 357,330		
interpolated boundary		
points: 10,408		

[†] here "PEG" is an abbreviation for the code "PEGASUS."

being simulated are generally much smaller than the time-step limits imposed by the DCF search restriction. This has been the case for all of the time-accurate moving body cases examined to date. However, an understanding of the DCF search restriction is important because it is illustrative of the basic concepts involved in unsteady chimera.

The DCF search restriction is depicted simply in Figure 3 by considering different movements of a hole in a one-dimensional grid. Three types of points are shown: hole points which are not part of the flow-field solution and are undefined, interpolated boundary points which contain interpolated flow values from a neighbor grid, and field points which are part of the flow field solution. Initially, a hole is defined in the one-dimensional grid by three consecutive node points as indicated in Figure 3a. Also indicated in the figure are interpolated boundary points on either end of the hole, and a number of field points. Figures 3b and 3c demonstrate two possible hole movements from the initial state shown in Figure 3a. Each of these movements occur in a single time-step. In Figure 3b, the hole moves to the right, causing the right hole boundary point to change from an interpolated boundary point to a hole point. Conversely, the movement causes the left hole boundary to become a field point and the left most hole point to become a interpolated hole boundary point. Though not shown in Figure 3, the exact reverse movement of that shown in Figure 3b is also possible. In either case, however, none of the hole points become field points. Therefore, this type of hole movement is valid. An

invalid hole movement is shown in Figure 3c, where the hole moves again to the right. In this movement, the right hole boundary point is shifted two node point locations to the right. The initial right hole boundary point and its immediate neighbor to the right (a field point) are now hole points. This is all valid. The violation occurs on the left hand side. The initial left hand boundary point and its immediate neighbor to the right become a field points. Hence, one point changed from a hole point to a field point without ever being updated through interpolation as a hole boundary point. The result of such a hole movement is to introduce undefined flow values into the field computation. Again, the time-step size limitation imposed by the DCF search limits are generally much less than those required to accurately resolve the physical processes being simulated.

The modifications to PEGASUS which resulted in the present DCF improve the DCF/ADF ratios (see Table 1) by a factor of ~ 3. Unfortunately, the DCF/ADF ratio is problem dependent, because the computational expense of the DCF is dependent on specific subdomain configurations, and some of the key DCF subroutines do not vectorize.

III. RESULTS

The prototype method has been applied to a set of test problems ranging from steady and unsteady moving body flow field solutions about simple airfoil sections, to a simulation of the integrated Space Shuttle vehicle during SRB separation. All computations were carried out on the NASA Numerical Aerodynamic Simulation Program (NAS) CRAY-2 super computers. The ADF used in this work was built on a coded version of algorithm (2) known as "VAPOR" [14]. However, the original VAPOR code neglected all of the terms associated with the time dependent metrics, $\xi_t, \eta_t,$ and ζ_t. The present ADF has been generalized accordingly. Therefore, the first results presented are those which were designed to verify the correctness of this generalization, and are carried out on single grid domains. The second set of computations presented were carried out with an emphasis on verifying the ADF's ability to use multiple grids and chimera logic to predict pressure loadings of a companion wind tunnel experiment for a wing and body combination at transonic conditions. The final set of computations presented below were intended as a first step in demonstrating the robustness of the overall prototype method (combined ADF, BDF, and DCF) in carrying out unsteady aerodynamic simulations of multiple bodies in relative motion for realistic three-dimensional configurations.

Verification of Generalization Made to the ADF

The ADF was applied to a pair of single-grid *inviscid* benchmark problems due to Magnus [15]. The first problem is for the solution about a NACA 64A010 airfoil at 1 degree angle of attack, and 0.8 free stream Mach number. The effect of angle of attack is achieved by plunging the airfoil at an equivalent constant rate, thus providing a preliminary check on the terms added into the ADF. The dimensionless plunge velocity is defined as

$$\xi_t = x_t\xi_x - y_t\xi_y - z_t\xi_z = 0$$
$$\eta_t = x_t\eta_x - y_t\eta_y - z_t\eta_z = 0$$
$$\zeta_t = x_t\zeta_x - y_t\zeta_y - z_t\zeta_z = -M_\infty sin(\tfrac{\pi}{180})$$

The present ADF result, which was run in a quasi 3-D mode (only 3 x-planes), is compared in Figure 4 with Magnus' results. The solution accuracy is good, though clearly the weak shock on the lower surface is diffused due to the coarseness of the grid in the vicinity of the shock.

A more definitive test of the time-metric related additions incorporated into the ADF is illustrated in Figure 5. In this second problem, the NACA 64A010 airfoil is sinusoidally plunged between +/- 1 degree. The amplitude of the dimensionless plunge velocity is defined as,

$$\xi_t = 0$$
$$\eta_t = 0$$
$$\zeta_t = -M_\infty sin(\tfrac{\pi}{180})sin(\bar{\psi})$$

where

$$\bar{\psi} = 2\pi\bar{t}/\bar{t}_p$$
$$\bar{t} = \text{dimensionless time}$$
$$\bar{t}_p = \text{dimensionless period of oscillation}$$
$$\bar{K} = \text{dimensionless reduced frequency} = 0.4$$

$\bar{K}$ is related to $\bar{t}_p$, by

$$\bar{t}_p = 2\pi/\bar{K}M_\infty.$$

Finally, $\bar{t}_p$ is related to the dimensional period of oscillation, t_p, as

$$t_p = \bar{t}_p L/a_o,$$

where a_o is the speed of sound.

Figure 5 shows excellent agreement for the lift coefficient (only the 4th cycle of oscillation is shown) between Magnus' and the present ADF's results.

Comparison of ADF and Wind Tunnel Data

A set of wind tunnel experiments sponsored by AFATL and carried out in the AEDC Aerodynamic Wind Tunnel (4T) provide the basis for a direct comparison between computed results from the present ADF and experimental data. The flow is for a minor body of revolution in close proximity to a generic wing. The body of revolution consists of a cylindrical center-section, and a tangent-ogive foresection and aftersection (see Figure 6a). The wing is

sting mounted, has a NACA 64A010 airfoil cross-section, and has span-wise symmetry about the root chord. One side of the wing is instrumented with a pressure tap matrix on both the upper and lower wing surfaces. The opposite side of the wing is intended for flow visualization. The body of revolution under the instrumented side of the wing is located beneath a pylon, is sting mounted, and is also instrumented with pressure taps. The body of revolution on the flow visualization side of the wing has no sting and is mounted directly to a pylon.

In the computation, the wing and body configuration is decomposed into two corresponding overset subdomains. The primary domain is defined with respect to the wing, and the subordinate domain is defined about the body of revolution (see Figures 6 b and c). This particular domain decomposition creates three inter-grid boundary conditions: two hole boundaries (i.e., wing hole in body grid, and body hole in wing grid), and an outer boundary for the body grid. The wing outer boundary is set to free-stream conditions, since the boundary is stretched far (10 chords) from the wing surface and nearby body of revolution. Symmetry boundary conditions are applied at the root chord in the wing grid, and no-slip conditions are applied at the wing and body surfaces.

It is possible to simulate the experimental configuration as given. However, the additional expense (more grid points) required to include the stings and pylon are not consistent with the objective of this test case (i.e., to *demonstrate* the combined elements of the prototype code). Accordingly, the pylon and stings are neglected in the present computations. In order to mitigate these geometric simplifications, and to maximize the opportunity to make direct comparisons with wind tunnel data, two configurations are presented: wing alone, and combined wing and body. The AFATL wing geometry is faithfully represented by the wing grid shown in Figures 6 b and c. The affect of the root chord sting in the experiment is certainly negligible over the instrumented section of the wing. Therefore, using the present wing grid, ADF results should agree well with experimental data for the first case. The geometric simplifications for the wing and body configuration (the second case) are clearly significant. Good agreement with experiment can be expected for the wing upper surface. However, neglect of the pylon will create significant differences on the wing lower surface and over most of the body surface.

Computed results for the two AFATL configurations are shown in Figure 7. Both configurations correspond to a Mach 1.05 free-stream at 2 degrees angle-of-attack, and a Reynolds number of 2.4 million per foot. The computed results for the wing alone case correspond well with the wind

tunnel pressure distributions, as expected. The combined wing and body results are in good quantitative agreement with the wind tunnel data for the wing upper surface. Differences between the computed solution and wind tunnel data over the wing lower surface and body surface are consistent with what was expected because of the geometric simplifications made in the computation (neglect of pylon and sting). Figures 8 and 9 are representative comparisons of wing pressure distributions between the two computed cases and the corresponding wind tunnel data sets. Figure 10 shows the computed and measured pressure distributions on the body of revolution.

Demonstration of the Prototype Method

The converged steady solution for the combined wing and body case described above provides initial conditions for a demonstration case of the present prototype method; the combined ADF, BDF, and DCF's. At time zero, the body is released from its position beneath the wing and traverses a prescribed path (recall that the BDF has not been implemented, hence the prescribed trajectory). The trajectory is constrained by a "pin" located at the body tail, leaving the nose free to trace a circular arc in the vertical direction. The body nose traverses downward one body diameter of arc length in 500 time-steps (150 milliseconds). Figure 11 illustrates snapshots of the unsteady solution at time zero, and again after 150, and 300 time-steps.

The final test case to be presented is a second demonstration of the prototype method, and involves the integrated space shuttle vehicle at SRB (solid rocket booster) separation. SRB separation occurs at just after two minutes into the flight at an altitude near 50,000 meters. For the purposes of this test, the following flight conditions are assumed:

$$M_\infty = 4.5$$
$$\alpha = +2°$$
$$R_e = 6.95x10^6$$

where the Reynolds number is based on the full-scale orbiter length.

The characteristic time scale for the problem is defined as the BSM (booster separation motor) burn time, which is approximately 2/3 sec. However, the effects of the BSM's on the flowfield are ignored to simplify the computation. As with the previous test case, a prescribed path for the separation process is also used here. In this case, the SRB separation path is chosen to mimic a trajectory that they could follow during the BSM burn-time. To reduce computer time, a simplified geometry model of the shuttle vehicle (see Figure 12) is used in which only the orbiter, ET (external tank), and SRB are represented *without* attach

hardware. A sting behind the orbiter is used to crudely model its plume, while the SRB body is closed off with a spherical cap. The composite grid contained approximately 350,000 points. The ET grid is treated as the primary grid, while the orbiter and SRB grids are subordinate. Overall, there are 8 inter-grid boundaries; including 2 outer boundaries (orbiter and SRB), and 6 hole boundaries (ET hole in SRB and orbiter, SRB hole in ET and orbiter, and orbiter hole in ET and SRB).

A sequence of plots from the time-accurate solution are shown in Figure 13 for times during the first characteristic time interval (i.e., $t = 0$, 0.34, and 0.68 sec., where $\Delta t = 1.36x10^{-3}$ sec.). The time interval was resolved with 500 points, and reveals a fascinating transient response in the pressure coefficient distribution over the surface of the integrated shuttle vehicle. As the SRB's move away from the ET and orbiter, the SRB bow shocks interact with the orbiter bow shock and impinge on the ET and orbiter surfaces causing localized zones of high pressure. As the SRB's continue to fall back and away, the high pressure zones correspondingly traverse back the length of the ET and orbiter.

IV. CONCLUSIONS

A prototype method has been presented for time-accurate simulation of three-dimensional multiple body viscous flows, given arbitrary grid combinations, body shapes, and relative motion between grid systems. The components of the method have been tested individually on benchmark cases, and collectively on realistic three-dimensional multiple body configurations. However, the effects of multiple subdomains and current intergrid boundary condition updating procedures on time-accuracy have not been addressed in this work. The obvious "weak-link" in the prototype method is the Body Dynamics Function, which is presently hardwired for prescribed trajectory cases. Development and testing of methods to address both of these issues are currently underway. Of course, further efforts to improve ADF and DCF efficiency are also planned.

There is currently some debate as to whether time-accurate Navier-Stokes simulations are even necessary for aerodynamics problems involving multiple bodies in relative motion. Quasi-steady type calculations are probably acceptable under certain circumstances for a number of configurations. However, there are probably many other situations for which the *pathological* cases can be predicted only with the aid of fully unsteady computational methods. The present prototype method, combined with dimensional reasoning and available data, will be used to explore this question further.

6

REFERENCES

1. Schwarz, H. A., Ueber einige Abbildungsaufgaben, J. Reine Angew. Math., 70, 105-120, 1869.

2. Dougherty, F. C. "Development of a Chimera Grid Scheme with Applications to Unsteady Problems," Ph.D. Dissertation, Stanford University, Stanford, CA, 1985.

3. Dougherty, F. C. and Kuan, J. H., "Transonic Store Separation Using a Three-Dimensional Chimera Grid Scheme," AIAA Paper No. 89-0637, Jan. 1989.

4. Steger, J. L., Dougherty, F. C., and Benek, J. A., "A Chimera Grid Scheme," Advances in Grid Generation, K. N. Ghia and U. Ghia, eds., ASME FED-Vol 5., June 1983.

5. Meakin, R. L. and Street, R. L., "Simulation of Environmental Flow Problems in Geometrically Complex Domains. Part 2: A Domain-Splitting Method," Comp. Meths. Appl. Mech. Engrg., 68, 311-331, 1988.

6. Atta, E. H. and Vadyak, J., "A Grid Interfacing Zonal Algorithm for Three-Dimensional Transonic Flows About Aircraft Configurations," AIAA Paper 82-1017, 1982.

7. Henshaw, W. D., "Part I: The Numerical Solution of Hyperbolic Systems of Conservation Laws, Part II: Composite overlapping Grid Techniques," Ph.D. Dissertation, Cal Tech, Pasadena, CA, 1985.

8. Glowinski, R., Dinh, Q. V., and Periaux, J., "Domain Decomposition Methods for Nonlinear Problems in Fluid Dynamics," Comp. Meths. Appl. Mech. Engrg., 40, 27-109, 1983.

9. Ying, S. X., Steger, J. L., Schiff, L. B., and Baganoff, D., "Numerical Simulation of Unsteady, Viscous, High Angle of Attack Flows Using a Partially Flux-Split Algorithm," AIAA Paper No. 86-2179, Aug. 1989.

10. Steger, J. L., Ying, S. X., and Schiff, L. B., "Partially Flux-Split Algorithm for Numerical Simulation of Compressible Inviscid and Viscous Flow," Workshop on Computational Fluid Dynamics, Institute of Non-Linear Sciences, U. of Calif., Davis, Calif., 1986.

11. Ying, S. X., "Three-Dimensional Implicit Approximately Factored Schemes for Equations in Gasdynamics," Ph.D. Thesis, Stanford, University. 1986.

12. Thomas, J. L., Taylor, S. L., and Anderson, W. K., "Navier-Stokes Computations of Vortical Flows Over Low Aspect Ratio Wings," AIAA Paper No. 87-0207, AIAA 25th Aerospace Sciences Meeting, Jan. 12-15, 1987.

13. Benek, J. A., Donegan, T. L., and Suhs, N. E., "Extended Chimera Grid Embedding Scheme with Application to Viscous Flows," AIAA Paper 87-1126-CP, 1987.

14. Buning, P. G., Chiu, I. T., Obayashi, S., Rizk, Y. M., and Steger, J. L., "Numerical Simulation of the Integrated Space Shuttle Vehicle in Ascent," AIAA Atmospheric Flight Mechanics Conference, Aug. 15-17, 1988.

15. Magnus, R. J., "Computational Research on Inviscid, Unsteady, Transonic Flow Over Airfoils," CASD/LVP 77-D10, Office of Naval Research, Jan. 1977.
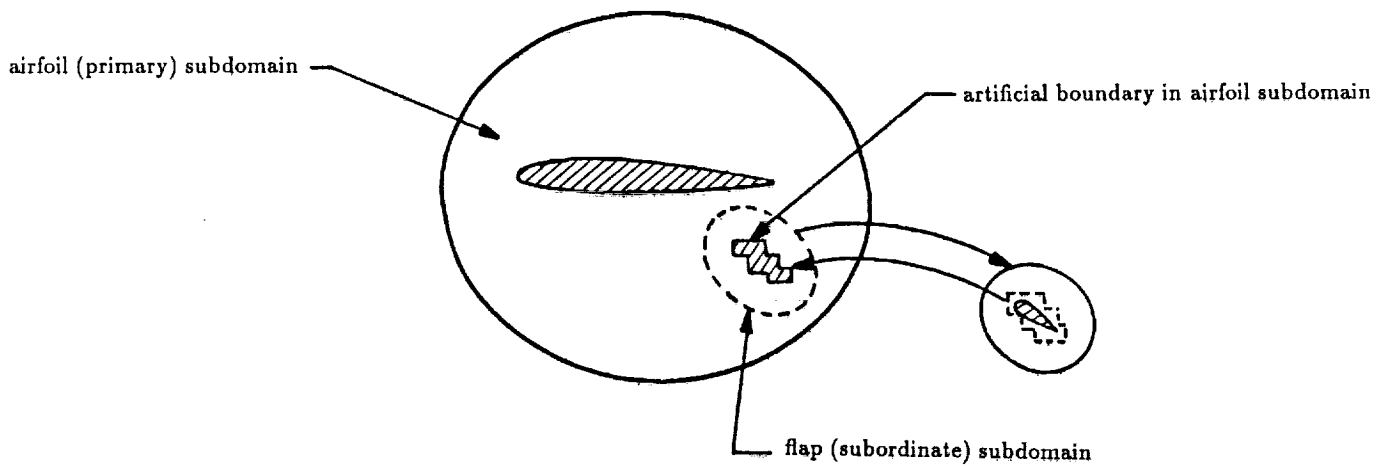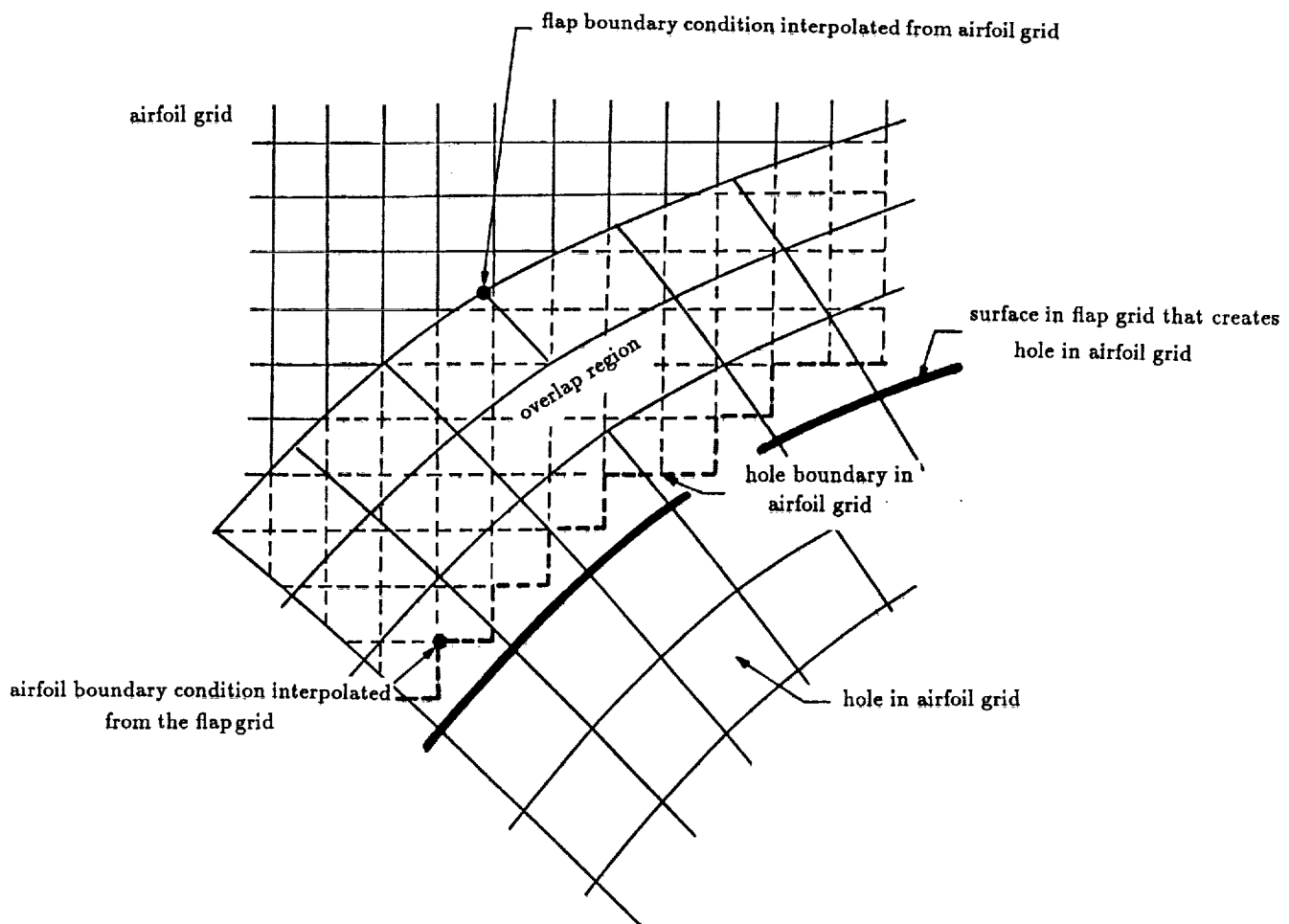
airfoil (primary) subdomain

artificial boundary in airfoil subdomain

flap (subordinate) subdomain

Figure 1. Inter-subdomain communication.

flap boundary condition interpolated from airfoil grid

airfoil grid

overlap region

surface in flap grid that creates
hole in airfoil grid

hole boundary in
airfoil grid

airfoil boundary condition interpolated
from the flap grid

hole in airfoil grid

Figure 2. Overlap region between subdomains. Discrete representation of the flapped airfoil problem.

8

initial hole location

a)

valid movement

b)

invalid movement

c)

—●— primary grid field point

—⊙— primary grid interpolated hole boundary point

—⊕— primary grid hole point

[- - - -] subordinate grid surface causing hole in primary grid
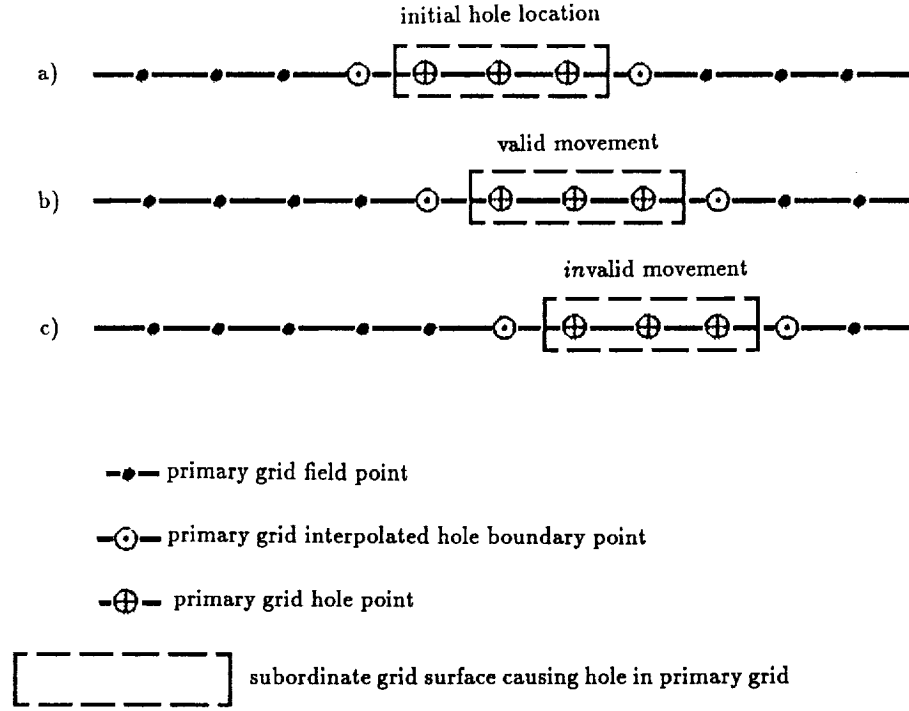
Figure 3. One-dimensional hole movement.
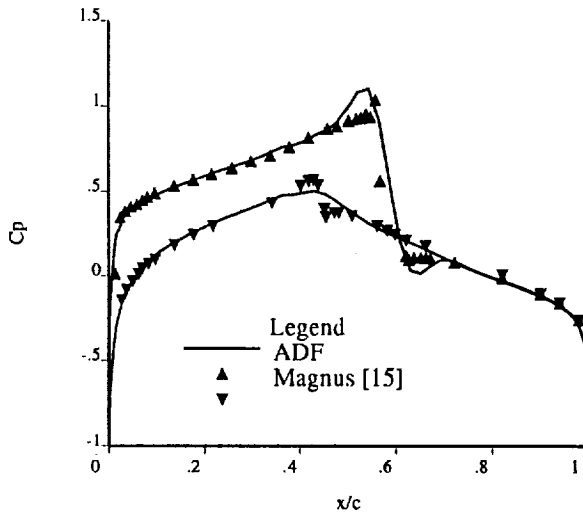
Figure 4. NACA 64A010 airfoil solution at a constant rate of plunge. $M_\infty = 0.8$, $\alpha = 0^\circ$, plunge $\sim \alpha = 1^\circ$. The present ADF (run inviscidly) vs. Magnus solution [15].
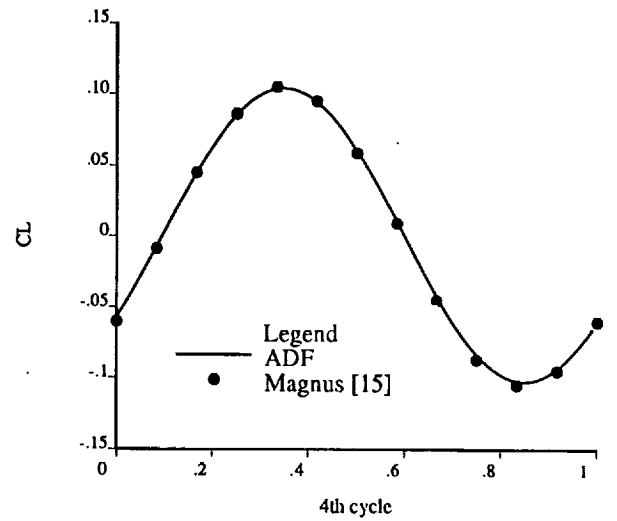
Figure 5. NACA 64A010 airfoil Cl variation during the fourth cycle of sinusoidal oscillation for a plunge $\sim \alpha = +/-1^\circ$. $M_\infty = 0.8$. The present ADF (run inviscidly) vs. Magnus solution [15].

b)

a)

c)
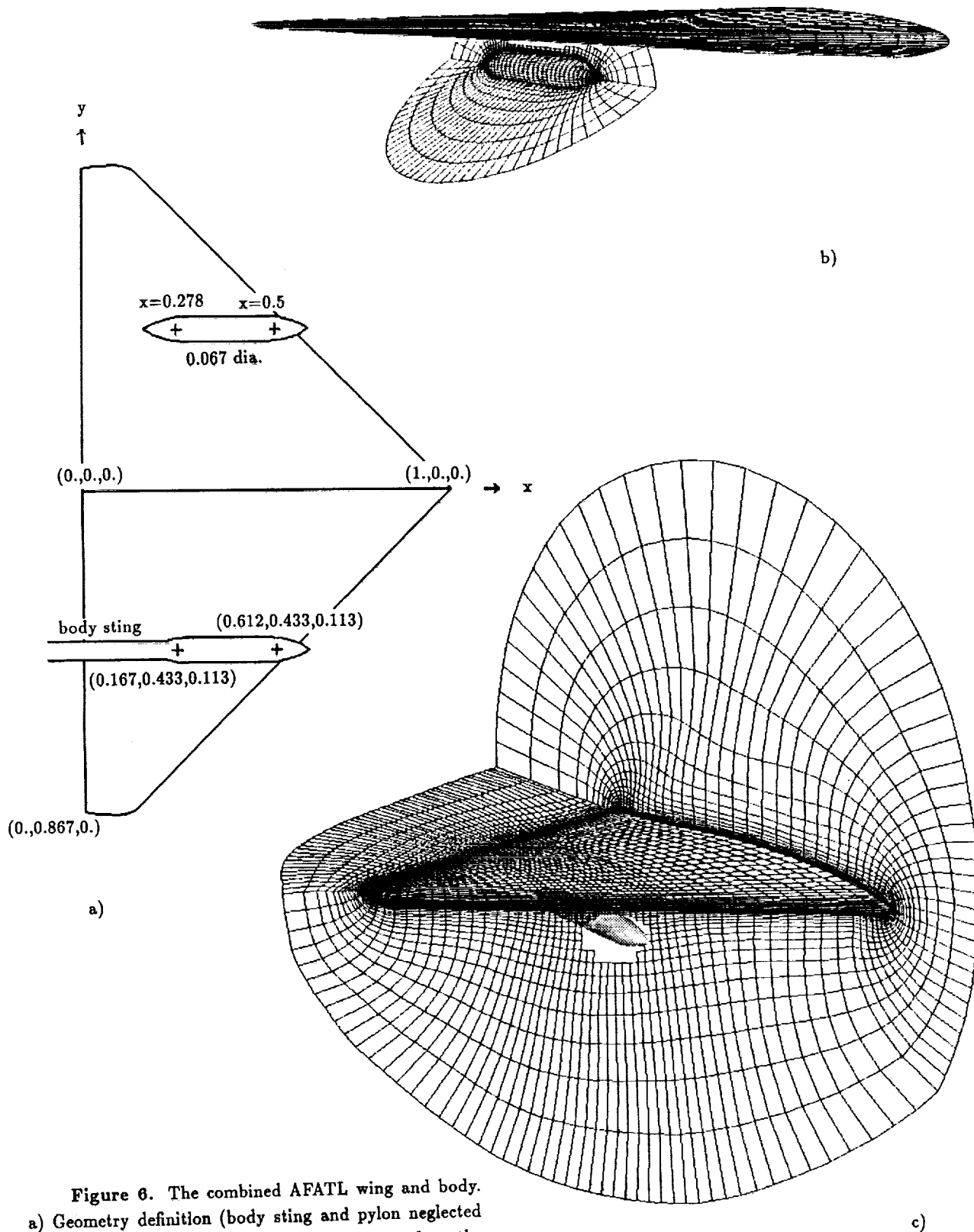
Figure 6. The combined AFATL wing and body.
a) Geometry definition (body sting and pylon neglected
in grids and computations). b) Selected surfaces from the
body grid (notice the hole caused by the wing grid). c)
Selected surfaces from the wing grid (notice hole caused
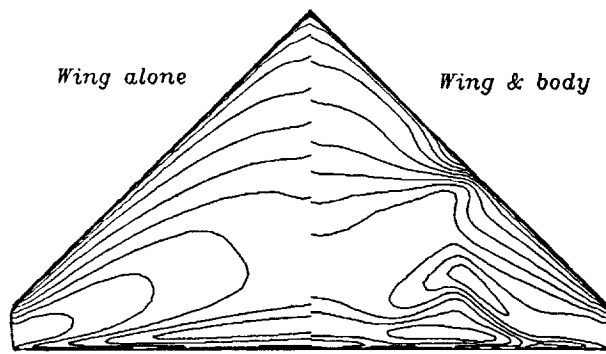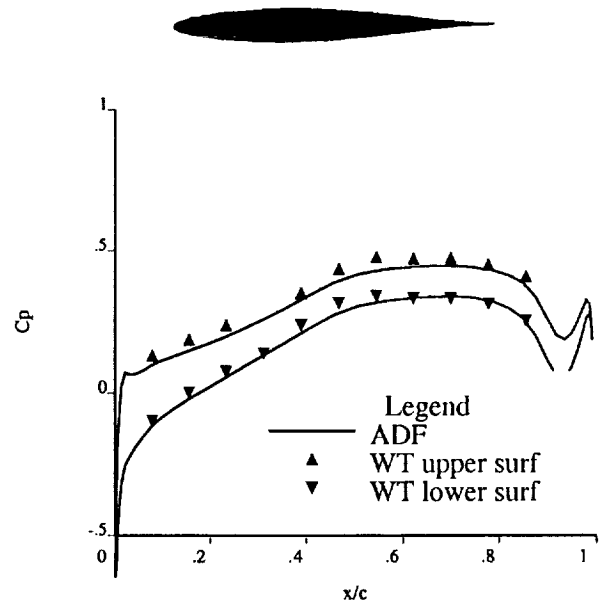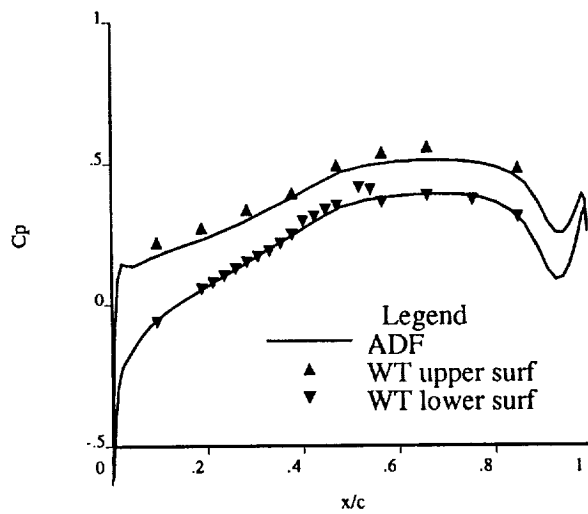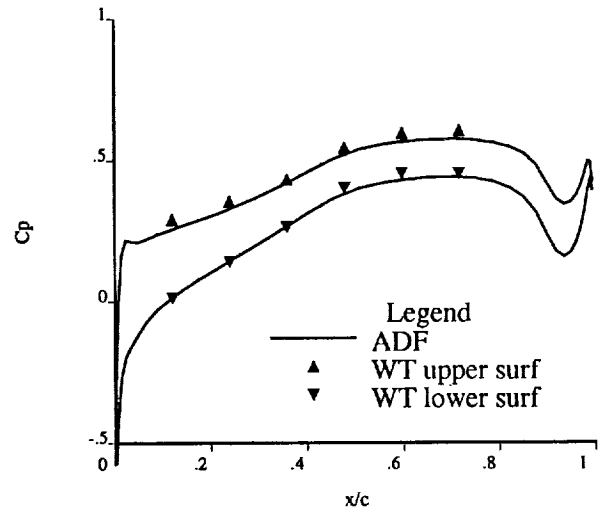by the body).

Figure 7. ADF Results: Comparison of pressure coefficient for the wing alone (left), and combined wing and body of revolution configuration (right). C_p contours are shown for the wing lower surface in both cases. $M_\infty = 1.05$, $\alpha = +2°$, and $R_e = 2.4x10^6/ft$.

a) C_p distribution at $y = 0.313$

b) C_p distribution at $y = 0.433$

c) C_p distribution at $y = 0.553$

Figure 8. Comparison of C_p for the wing alone case. ADF results versus wind tunnel data. $M_\infty = 1.05$, $\alpha = +2°$, and $R_e = 2.4x10^6/ft$.

11

a) C_p distribution at $y = 0.313$

Legend
— ADF (no pylon)
▲ WT upper surf
▼ WT lower surf

b) C_p distribution at $y = 0.433$

Legend
— ADF (no pylon)
▲ WT upper surf
▼ WT lower surf

c) C_p distribution at $y = 0.553$

Legend
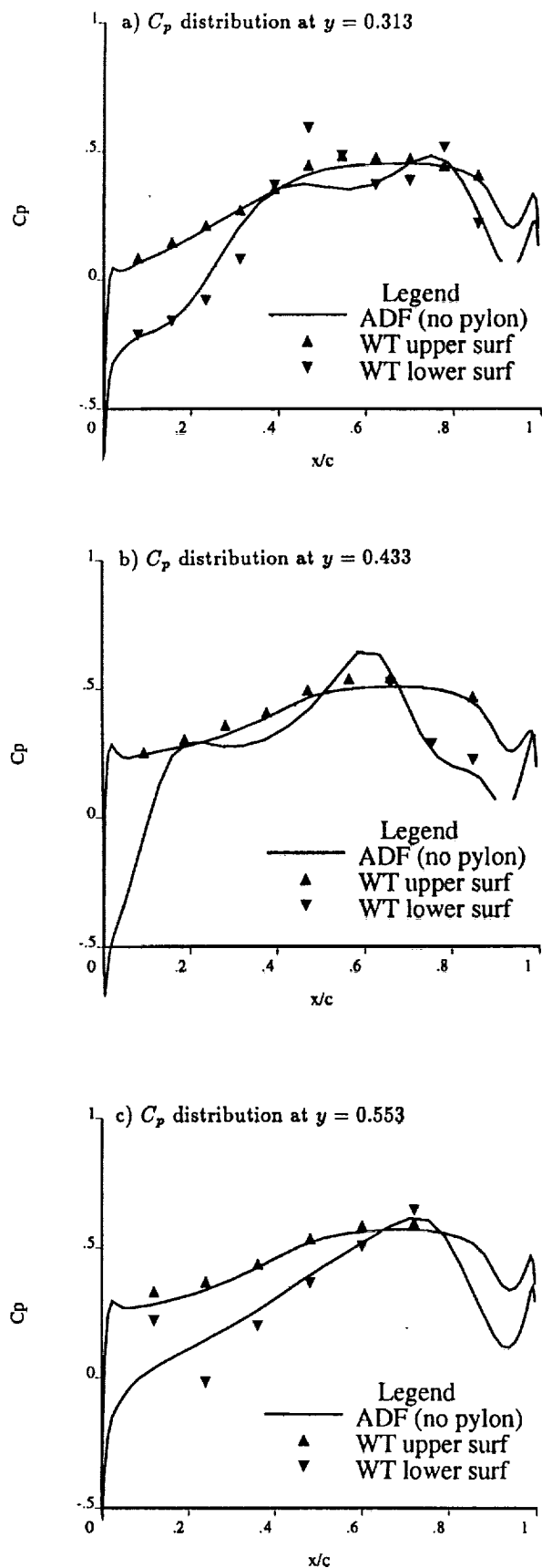— ADF (no pylon)
▲ WT upper surf
▼ WT lower surf

Figure 9. Comparison of C_p for the combined wing and body case: 3 wing sections at locations "y" from the root chord. ADF results versus wind tunnel data. $M_\infty = 1.05$, $\alpha = +2°$, and $R_e = 2.4x10^6/ft$.

a) C_p distribution at $\theta = 0°$
(facing the wing lower surface).

Legend
— ADF (no pylon)
▲ WT upper surf

b) C_p distribution at $\theta = 180°$.

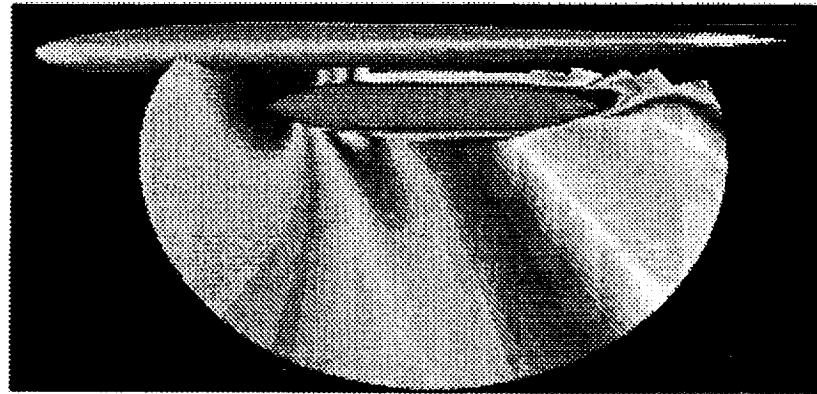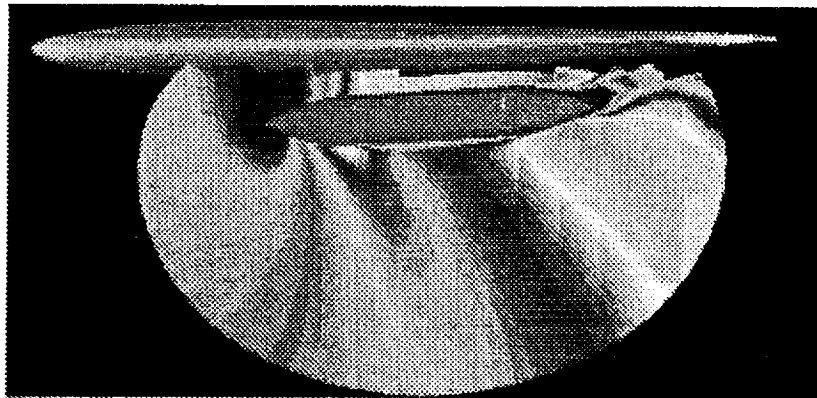**Legend**
— ADF (no pylon)
▼ WT lower surf
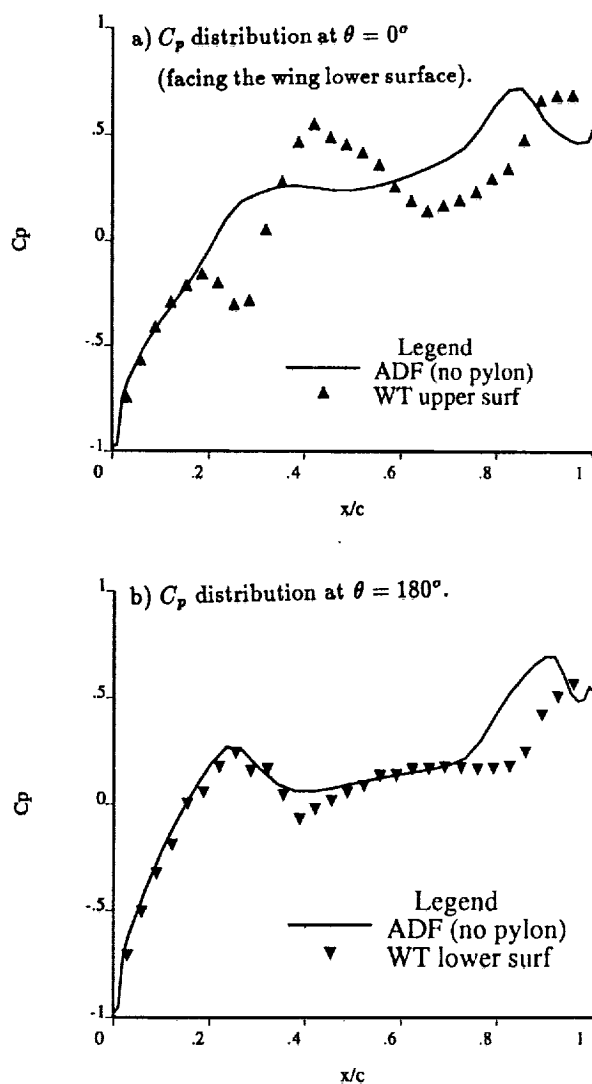
Figure 10. Comparison of C_p about the body of revolution. ADF results versus wind tunnel data. $M_\infty = 1.05$, $\alpha = +2°$, and $R_e = 2.4x10^6/ft$.
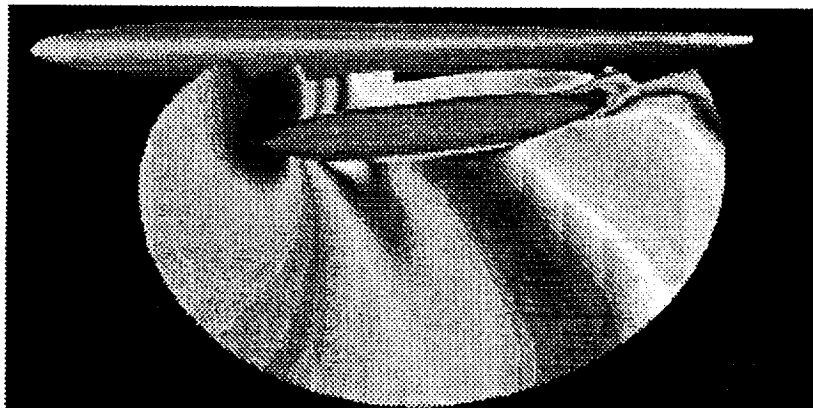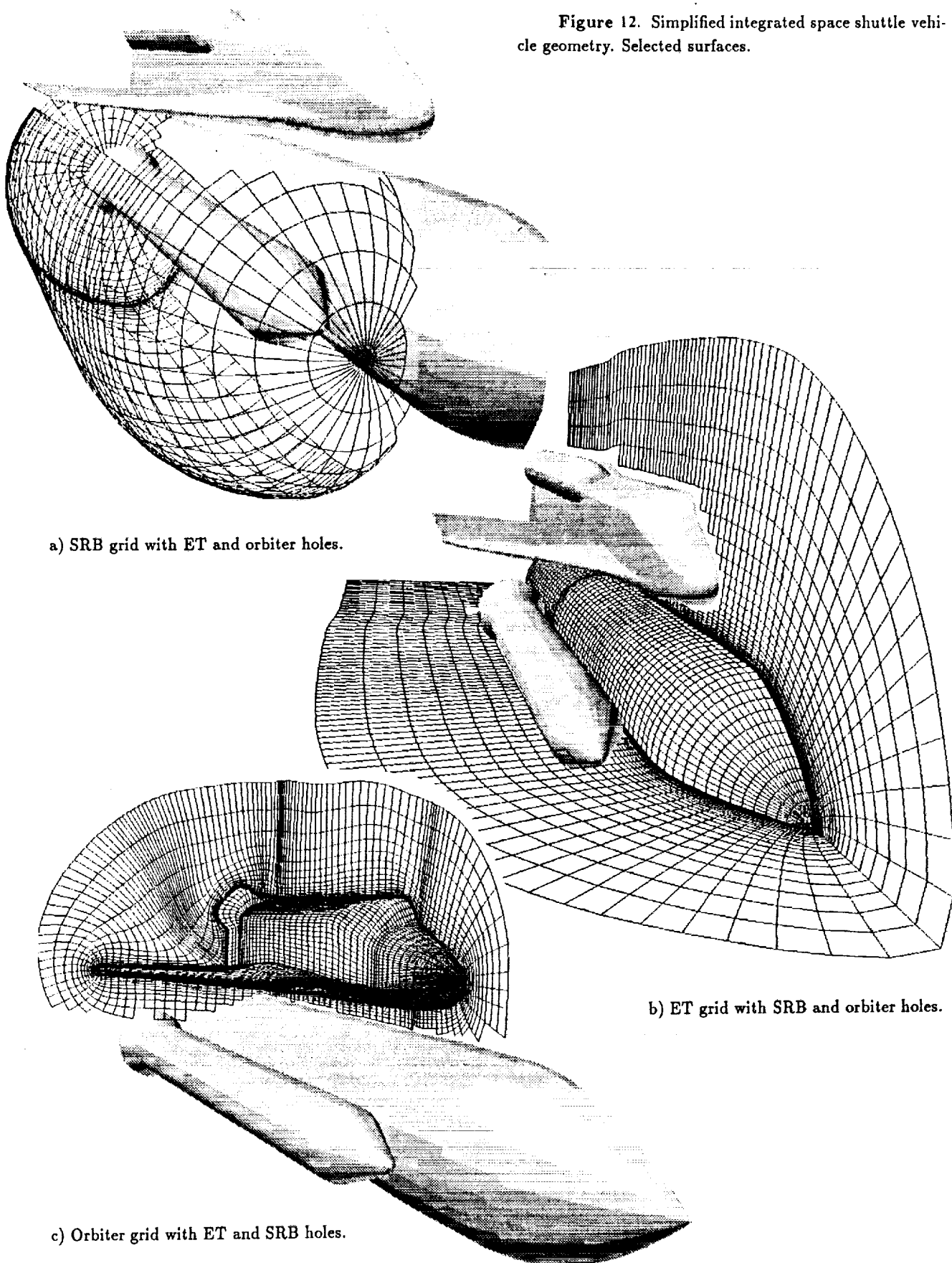
12

a) $t = 0$

b) $t = 45$ msec.

c) $t = 90$ msec.

Figure 11. Prototype Program Demonstration Case. Mach contours about the body of revolution during a hypothetical separation sequence from the wing. $M_\infty = 1.05$, $\alpha = +2°$, and $R_e = 2.4x10^6/ft$.

13

Figure 12. Simplified integrated space shuttle vehicle geometry. Selected surfaces.

a) SRB grid with ET and orbiter holes.

b) ET grid with SRB and orbiter holes.

c) Orbiter grid with ET and SRB holes.
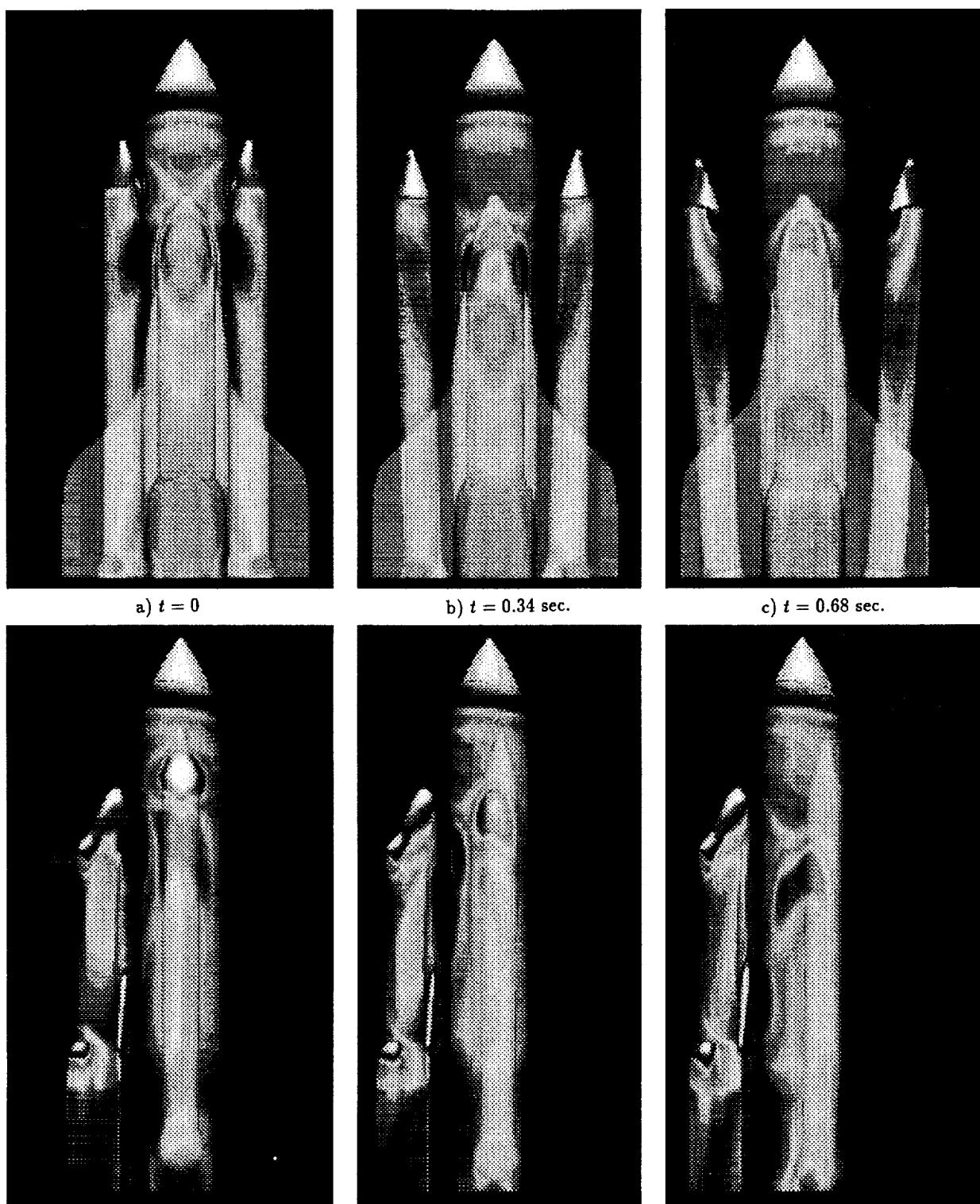
14

a) $t = 0$ b) $t = 0.34$ sec. c) $t = 0.68$ sec.

Figure 13. Prototype Program Demonstration Case.
C_p contours about the integrated space shuttle vehicle during SRB separation. In the top views, the orbiter is transparent. Likewise, the SRB is transparent in the side views.
$M_\infty = 4.5$, $\alpha = +2°$, and $R_e = 6.95x10^6$.

15

NASA National Aeronautics and Space Administration	Report Documentation Page		
1. Report No. NASA TM-102181	2. Government Accession No.		3. Recipient's Catalog No.
4. Title and Subtitle Unsteady Aerodynamic Simulations of Multiple Bodies in Relative Motion: A Prototype Method			5. Report Date July 1989
			6. Performing Organization Code
7. Author(s) Robert L. Meakin (Sterling Federal Systems, Inc.)			8. Performing Organization Report No. A-89095
			10. Work Unit No. 505-60
9. Performing Organization Name and Address Ames Research Center Moffett Field, CA 94035			
			11. Contract or Grant No.
12. Sponsoring Agency Name and Address National Aeronautics and Space Administration Washington, DC 20546-0001			13. Type of Report and Period Covered Technical Memorandum
			14. Sponsoring Agency Code

15. Supplementary Notes

16. Abstract

A prototype method for time-accurate simulation of multiple aerodynamic bodies in relative motion is presented. The method is general and features unsteady chimera domain decomposition techniques and an implicit approximately factored finite-difference procedure to solve the time-dependent thin-layer Navier-Stokes equations. The method is applied to a set of two- and three-dimensional test problems to establish spatial and temporal accuracy, quantify computational efficiency, and begin to test overall code robustness.

17. Key Words (Suggested by Author(s)) Chimera Unsteady, Thin-layer Navier-Stokes Space Shuttle Store separation	18. Distribution Statement Unclassified-Unlimited Subject Category: 02		
19. Security Classif. (of this report) Unclassified	20. Security Classif. (of this page) Unclassified	21. No. of pages 17	22. Price A02